CONVERTING WIND ENERGY INTO ELECTRICAL ENERGY USING RESONANT WIND GENERATORS, A COMPARATIVE STUDY

Firas HUSSANY * ⓘ, **Jasim AL-BEDHANY** ⓘ, **Mahmood S. MAHMOOD** ⓘ

University of Misan, Iraq
* Corresponding author, e-mail: firaslattef@uomisan.edu.iq

Abstract

The limitations of traditional energy sources and the harmful environmental impacts resulting from their investment have prompted many researchers to seek clean and renewable energy resources, in this research, a comparative study was conducted using computational fluid dynamics between two models of resonant bladeless wind generators having similar mass and material in order to study the effect resulting from the design profile on the aerodynamic performance, the frequency response, and then its impact on the power generated, fSI (Fluid structure interaction) numerical modelling was performed using Ansys 16.1 software, by first modelling the flow field around the generator using the LES (Large Eddy simulation) turbulence pattern and then calculating the forces acting on the body and the frequencies resulting from the vibration of the vortices around the body, the analyses linking with the body by analyzing the mutual interaction between the fluid and the body using one-way fluid-structure interaction coupling with (FSI)to study the vibrations resulting from the vortices and hence the energy can be produced from them, the study showed a noticeable improvement in the aerodynamic performance of the second modified model compared to the first, as the lift coefficient increased by 49.3%, while the drag coefficient decreased by 34%,On the other hand, the frequency ratio decreased in the second model by 2.3%, and this led to a significant increase in generated power in the second model compared to with the first one.

Keywords: lift coefficient; drag coefficient; frequency ratio; frequency response; numerical modelling

1. INTRODUCTION

The increasing demand of energy and the environment challenge pushes towards the use of renewable energy, especially wind energy. The classic use of horizontal and vertical axes of wind turbine open the door in front of extended use of renewable energies such as hydraulic waves of seas and oceans and the use of a new use of resonance of rods connecting to generators throughout the pass of wind or water [1]. Advancements in harnessing wind energy extend beyond conventional bladed turbines to encompass innovative technologies like resonant wind generators, which leverage the phenomenon of flow-induced vibration, specifically vortex-induced vibration (VIV), for energy conversion [2]. These bladeless generators present potential advantages in terms of structural simplicity and reduced maintenance due to the absence of complex rotating machinery like blades and gearboxes. However, a critical limitation hindering their widespread adoption such as the relatively low power output and the sensitivity of energy generation to variations in the vibrating structure's profile along its height. This necessitates a deeper understanding of their operational characteristics and performance under diverse environmental conditions.

The estimated potential worldwide power of wave resource is ~2 TW [3]. In the UK's realistic potential, this power being 7–10 GW [4] of the UK's total capacity of grid with 80 GW, with peak load demand stabilized with around 65 GW. As such, up to 15% of current UK electricity requirement could be met using wave energy. When combined with the generation tidal stream, up to 20% of the UK requirement could be met [5] This clearly refers to the importance of wave energy as an important source of renewable energy can be sufficiently used to cover the increasing demand of energy.

The fundamental principle behind resonant wind generators lies in the interaction between a fluid flow and a bluff body, leading to flow-induced vibration (FIV), a common manifestation of FIV is vortex-induced vibration (VIV), which arises when alternating vortices are shed from the sides of a non-streamlined object immersed in a flow at a specific velocity. the periodic vortex shedding creates fluctuating pressure distributions around the object,

leading to an inducing of oscillatory motion (Figure 1) [6].
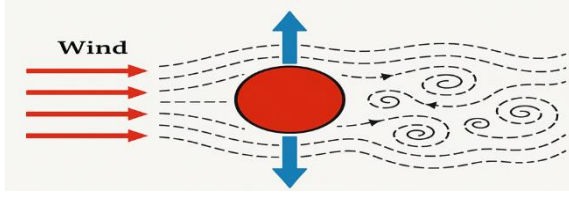

Fig. 1. Flow induced vibration.

To effectively harness VIV for energy generation, a thorough understanding of the fluid-structure interaction is paramount. The most important characteristic in describing a fluid flow is Reynolds number (Re). It related viscosity, velocity and media of flow. Consider the classic case of flow past a circular cylinder, at very low Reynolds numbers (Re < 0.5), viscous forces dominate, and the flow remains attached, exhibiting no separation or vortex formation (Figure 2-a) [7], as the Reynolds number increases (2 < Re < 30), the flow separates at the rear of the cylinder, forming a pair of stationary counter-rotating vortices in the near wake (Figure 2-b) [7], these vortices extract energy from the main flow, representing an energy dissipation mechanism.

Around a Reynolds number of 90, these stationary vortices become unstable and begin to detach and move downstream alternately, in the range of 40 < Re < 70, the wake behind the cylinder starts to oscillate periodically, with the frequency and amplitude of these oscillations increasing with rising Reynolds numbers up to approximately 90 (Figure 2-c) [7, 8]. Beyond this critical Reynolds number, a continuous and alternating shedding of vortices occurs, forming the well-known von Kármán vortex street in the cylinder's wake (Figure 2-d and e) [9].
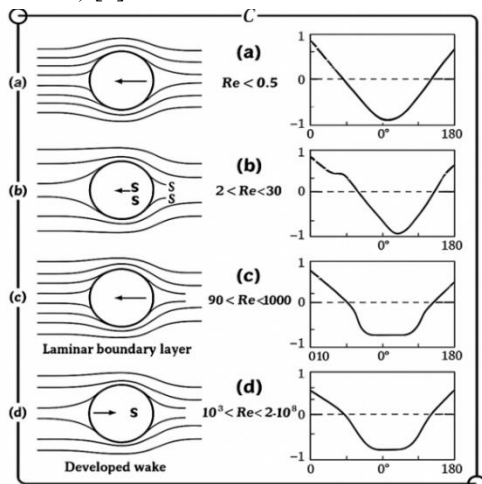

Fig. 2. Vortex formation and pressure coefficient with Reynolds number

The width of this wake is directly influenced by the location of the boundary layer separation point; earlier separation results in a wider wake, turbulent boundary layers exhibit greater resistance to

separation compared to laminar layers due to enhanced momentum transfer within the fluid, the frequency (f) of this vortex shedding can be estimated using the empirical relationship:

$$St = \frac{\{fd\}}{\{U_o\}} = 0.198 \left(1 - \frac{\{19.7\}}{\{Re\}}\right) \quad (1)$$

where St is the Strouhal number, d is the characteristic length (e.g., cylinder diameter), and U_o is the free stream velocity, this formula is generally applicable for Reynolds numbers in the range of $250 < Re < 2 * 10^5$ [6-8]. While resonant wind generators offer potential advantages such as design simplicity and the absence of complex mechanical components, their primary limitations lie in the low power output and the significant impact of the vibrating structure's geometry along its height on energy generation. Furthermore, this study focuses extensively on the academic explanation of von Kármán vortex shedding and general fluid flow phenomena around a cylinder [9],

In this study, two models will be analysed to compare their response to the stream of wind and the generated power from each model. This can provide a powerful selection between different models to have an efficient structure of power generation system using resonance of wind and vibration.

2. ANALYTICAL AND GOVERNING EQUATIONS

Computational Fluid Dynamics(CFD), is one of the powerful tools used in modelling involving the flow of fluids, which extends to a wide number of application fields in aerodynamics, industrial engineering, chemical processes, electrical, marine, environmental engineering and other applied sciences that enter into various areas of life, there are many commercial programs that use this science to analyze and solve engineering systems, one of the most important of which is Ansys Fluent, solving the problem numerically in this software includes solving a set of differential equations that describe the fluid movement, these equations include the continuity and momentum equations, which can be expressed by the following relationships [11,12]:

continuity equation

$$\frac{\partial \rho}{\partial t} + \frac{\partial(\rho u)}{\partial x} + \frac{\partial(\rho v)}{\partial y} + \frac{\partial(\rho w)}{\partial z} = 0 \quad (2)$$

x- momentum

$$\rho\left(\frac{\partial u}{\partial t} + u\frac{\partial u}{\partial x} + v\frac{\partial u}{\partial y} + w\frac{\partial u}{\partial z}\right) = -\frac{\partial p}{\partial x} + \rho g_x + \mu\left(\frac{\partial^2 u}{\partial x^2} + \frac{\partial^2 u}{\partial y^2} + \frac{\partial^2 u}{\partial z^2}\right)$$

y- momentum

$$\rho\left(\frac{\partial v}{\partial t} + u\frac{\partial v}{\partial x} + v\frac{\partial v}{\partial y} + w\frac{\partial v}{\partial z}\right) = -\frac{\partial p}{\partial y} + \rho g_y + \mu\left(\frac{\partial^2 v}{\partial x^2} + \frac{\partial^2 v}{\partial y^2} + \frac{\partial^2 v}{\partial z^2}\right)$$

z- momentum

$$\rho\left(\frac{\partial w}{\partial t} + u\frac{\partial w}{\partial x} + v\frac{\partial w}{\partial y} + w\frac{\partial w}{\partial z}\right) = -\frac{\partial p}{\partial z} + \rho g_z +$$
$$\mu\left(\frac{\partial^2 w}{\partial x^2} + \frac{\partial^2 w}{\partial y^2} + \frac{\partial^2 w}{\partial z^2}\right) \qquad (3)$$

Where P represents pressure, μ viscosity, g is the gravitational acceleration, ρ density. And $u.v.w$ Components of the velocity on the x, y, and z axes respectively.

The Navier-Stokes equations for the basic flow components can be solved more efficiently when the flow properties change over large scales compared to these properties change over small scales, therefore, the turbulence model LES (Large dEdy Simulation) depends on reformulating the Navier-Stokes equations, considering the flow components within cell dimensions and appropriate temporal changes can be captured, it can be solved directly but, the changes that occur within the cell that cannot be reached will be treated and approached by one of the turbulence model.

When observing the energy spectrum of the flow structure, it is possible to observe a volume of fluid with large energy and another volume with small energy, the energy is proportional to the flow speed; therefore, the component of the instantaneous velocity can be analyzed into two components, as in the followed equation [13]:

$$u_i(\vec{x}.t) = \overline{u_i}(\vec{x}.t) + u'_i(\vec{x}.t) \qquad (4)$$

Where the terms $u_i(\vec{x}.t)$ represents the component of the instantaneous velocity, $\overline{u_i}(\vec{x}.t)$ represents the component of the speed within the scale that can be analyzed, while the term $u'_i(\vec{x}.t)$ represents the structure of the flow with a small speed that cannot be analyzed, therefore, the Navier-Stokes equation can be written as follows [13]:

$$\frac{\partial \overline{u_i}}{\partial t} + \frac{\partial \overline{u_i u_j}}{\partial x_j} = -\frac{1}{\rho}\frac{\partial \bar{p}}{\partial x_i} + \frac{\partial}{\partial x_j}\left(v\frac{\partial \overline{u_i}}{\partial x_j}\right) - \frac{\partial \tau_{ij}}{\partial x_j} \qquad (5)$$

$$\tau_{ij} = \rho\left(\overline{u_i u_j} - \overline{u_i}\,\overline{u_j}\right) \qquad (6)$$

3. NUMERICAL MODELLING

The movement of the cylinder under the influence of fluid movement can be considered as a forced vibrating system under the influence of the lift and drag forces which damped by the viscosity of the air can be represented as a spring and damper system as can be seen in Fig. *3* [14].

Harmonic analysis of the frequency response occurs when the body is subjected to a variable force of a reciprocating nature of the form $F = F_o \sin(\omega t)$, where F_o represents the amplitude of the force, ω represents the frequency of application of the force, and the natural angular frequency of any vibrating system is given by the relationship $\omega_n = \sqrt{\frac{k}{m}}$ [15].

Where k is the stiffness constant or equivalent stiffness and m is the mass. While the natural frequency is $f_n = \frac{\omega_n}{2\pi}$ with unit of Hz.

The vibration equation of a cylinder under the influence of air movement around it is given by [16]:

$$m\ddot{\theta} + c\dot{\theta} + k\theta = F_o \sin(\omega_s t) \qquad (7)$$

Where ω_s represents the frequency of the vortices, this pendulum movement can be transferred to linear motion in a direction perpendicular to the pendulum arm to get the system shown in Fig. *3* and the equation of motion can be rewritten as:

$$m\ddot{y} + c\dot{y} + ky = F_o \sin(\omega_s t) \qquad (8)$$

This equation has a special solution of the form $= A\sin(\omega_s t + \emptyset)$) where A represents the amplitude of the vibration amplitude and is given by the relationship [16]:

$$A = \frac{F_o}{K\sqrt{\left(1-\left(\frac{\omega_s}{\omega_n}\right)^2\right)^2 + \left(2\xi\left(\frac{\omega_s}{\omega_n}\right)\right)^2}} \qquad (9)$$

ξ From the previous relationship represents the damping ratio and is given by $= C/C_c$, where C_c represents the critical damping value and is given by the relationship $C_c = 2m\omega_n$, according to the value of C_c; there are three cases:

- $C > C_c$ It is a state of strong damping and the movement has no vibration.
- $C = C_c$ It is a state of critical damping and movement at the border between vibration and creep.
- $C < C_c$ It is a state of vibrating movement.

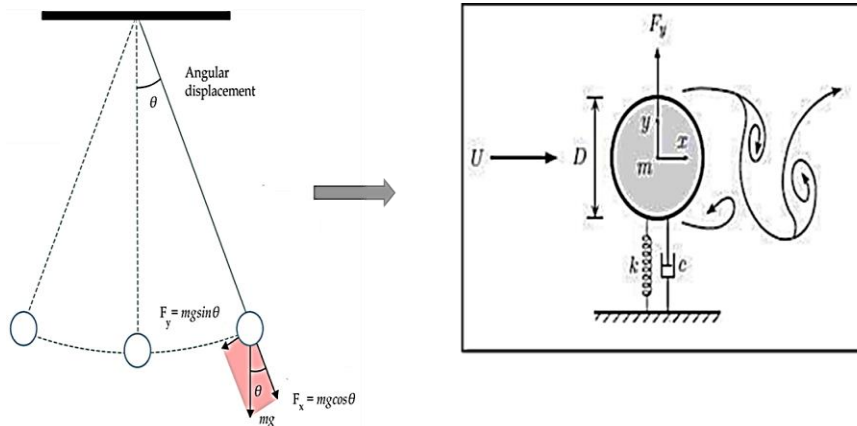Therefore, the condition for vibrating motion is when $\xi < 1$.

Fig. 3. The cylinder is vibrating system

∅ represents the phase difference between the applied force and the displacement resulting from the movement of the body and is given by:

$$\emptyset = tg^{-1}\left(\frac{2\xi\left(\frac{\omega_s}{\omega_n}\right)^2}{1-\left(\frac{\omega_s}{\omega_n}\right)^2}\right) \qquad (10)$$

The acting resultant force consists of two forces: lift and drag [17].

Lifting force: This force is characterized by a vibrational nature, which is given by the relationship:

$$F_L = \left(\frac{1}{2}\rho U^2 SCl_o\right)_{F_{L(Amplitude)}} \sin(\omega_s t + \varphi) \quad (11)$$

Where $\omega_s = 2\pi f$ represents the angular vibration frequency (rad/sec) and φ the phase angle, and the Root Mean Square (RMS) of the lifting force can be computed as:

$$F_{l(RMS)} = 0 \cdot 707\, F_{L(Amplitude)} \qquad (12)$$

The drag force is an almost constant force, or its fluctuation can be neglected and its average value over time can be adopted by the relationship [19,20]:

$$F_{d(Avg)} = \frac{1}{2}\rho U^2 SCd_{(Avg)} \qquad (13)$$

Therefore, the total (resultant) force is:

$$F_{(Amplitude)} = \sqrt{F^2_{L(Amplitude)} + F^2_{d(Avg)}} =$$
$$\frac{1}{2}\rho U^2 S \sqrt{Cl^2_{(Amplitude)} + Cd^2_{(Avg)}} \qquad (14)$$

The power is given by $= F_{RMS} \times U_{RMS}$, where U_{RMS} is the root mean square value of the body's displacement speed and represents the derivative of the displacement with time and is given by the relationship:

$$U = \frac{dX}{dt} = \left(X_{Ampltidude}\omega_s\right)_{U_{amplitude}} \cos(\omega_s t + \varphi) \qquad (15)$$

Therefore, the root mean squared value of the velocity is:

$$U_{RMS} = 0 \cdot 707\, X_{Ampltidude}\, 2\pi f_s \qquad (16)$$

The value of the displacement amplitude can be linked to the vibration frequency, natural frequency, and damping ratio by the relation:

$$X_{Ampltidude} = \frac{1/2\rho U^2 SCl_{RMS}\cos\beta}{K\sqrt{\left(1-\left(\frac{f_s}{f_n}\right)^2\right)^2 + \left(2\xi\frac{f_s}{f_n}\right)^2}} \qquad (17)$$

Whereas $K = \omega^2_n m$, it is the stiffness constant and β is the angle between the column and the direction of impact of the resultant force resulting from lift and drag as in Fig. 4[17].
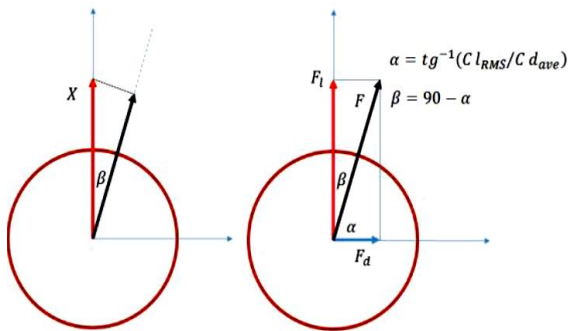

Fig. 4. Angle in power equation

Then the total power relationship is:

$$P = (1/2\,\rho U^2 S)^2 \sqrt{Cl^2_{(Amplitude)} + Cd^2_{(Avg)}}$$
$$\frac{Cl_{RMS}\cos\beta}{K\sqrt{\left(1-\left(\frac{f_s}{f_n}\right)^2\right)^2 + \left(2\xi\frac{f_s}{f_n}\right)^2}}\,2\pi f_s \qquad (18)$$

Angle α (Figure 4) is derived from the relationship between the lift and drag forces generated by the interaction between the wind and the vibrating column, according to the inverse tangent of the ratio of the root mean square of the lift coefficient $\left(C_{l_{\{RMS\}}}\right)$ to the average drag coefficient $\left(C_{d_{\{ave\}}}\right)$, the root mean square of the lift coefficient reflects the temporal fluctuations of the lift force due to vortex shedding, while the average drag coefficient represents the horizontal resistance of the column, this angle α defines the direction of the total aerodynamic force acting on the column, angle β, on the other hand, is the complement of α and is given by 90 degrees minus α. B represents the angle between the vertical axis of the column and the direction of the total aerodynamic force (Figure 4), a larger β indicates a greater horizontal component of the total force, which enhances the horizontal vibrations of the column – a crucial factor in improving energy conversion efficiency [17].

- Total Power Equation and the Influence of Dynamic Factors

ρ is the air density, U is the free wind speed, S is the area exposed to the wind, amplitude is the oscillation amplitude of the column, arg is the relative phase of oscillation between the force and motion, and $l_{\{RMS\}}$ is the root mean square of the effective column length, the square root term, $\sqrt{\{C_l^2 + C_d^2\}}$, represents the nonlinear interaction between lift and drag forces, where the dominance of the lift force becomes prominent when the vibration frequency increases in synchronization with the vortex shedding frequency.

The stiffness constant K is given by the relationship $K = wa_n^2.m$, where wa_n is the natural frequency of the column and m is the mass of the system. Resonance occurs when the vortex shedding frequency (given by the Strouhal number $St = \frac{\{fD\}}{\{U\}}$ matches the natural frequency of the column (w_n), leading to amplified oscillation amplitudes and increased extracted power, in this scenario, the angle β becomes a pivotal factor in achieving synchronization between the two frequencies [17], in the proposed model (Figure 5), the gradual tapering of the column diameter with height reduces the lock-in loss phenomenon resulting from the variation of wind speed with altitude, this design improves surface pressure distribution and minimizes random vortex shedding, thereby increasing the stability of oscillations and enhancing energy conversion efficiency by up to 30% compared to the traditional model [2], improving the angle β by enhancing the $\frac{C_l}{C_d}$

ratio (e.g., using serrated surfaces) increases the generated power, designing tapered columns limits the impact of vertical wind speed gradients on vortex synchronization, two-way fluid-structure interaction (Full FSI) modeling is essential to avoid overestimating power in simplified models.

4. GEOMETRY AND BOUNDARY CONDITIONS

In this research, two models have been studied, the dimensions of one were taken from previous studies, while the other proposed design was drawn according to dimensions related to those of the first model, so that they have approximately equal mass. Both models are hollow with a thickness 10 mm, the study will be carried out at a wind speed of 5 m/s and *Figure 5* shows the drawn dimensions of each model.
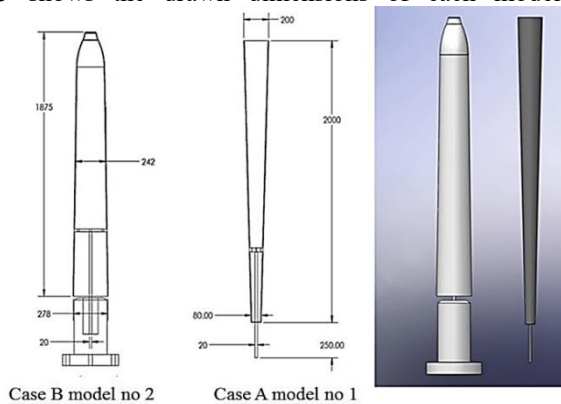

Figure 5. Cases studied.

The flow field of the fluid surrounding the surface of the studied body will first be modelled as a transient state of (CFD) using Ansys Fluent 16.1 software, which relies in principle on the Finite Volume Method (FVM), the flow field values were calculated using the LES turbulence model and averaging the values changing with time. Using the arithmetic mean and the root mean square (RMS) of values in order to calculate the forces exerted by the flow field on the surface of the body, these forces are lift and drag forces, and then calculate the vortex shedding frequency in each case.

Based on the values and frequencies of the calculated forces from the flow field, the frequency response study of the effect for those forces on the body' surface was conducted to determine the values of the vibration amplitudes and the power can be extracted by the body from the flow field, this study was carried out using static and dynamic analysis using Ansys workbench software, for the two used models, by calculating the natural frequencies of the studied geometric models, then the Dynamic Response Software (DRS), has been used, which takes the results of the first program to calculate and draw the frequency response diagrams of the studied body.

Modelling the phenomenon of vortex shedding requires a computational mesh with very precise

specifications, since the phenomena occur within the dimensions of the boundary layer, including a pressure fluctuation near the surface of the body and separation of the boundary layer, these small changes have significant impact on the entire flow field, thus, the generating mesh based on criteria that express the accuracy of the mesh, the y^+ value also monitor during the solution to keep its value not exceeding one, the height value of the first cell near the surface of the studied object has been calculated, which gives a value $y^+ \leq 1$. By using the turbulence model LES forces to smooth the mesh in the region at the vortices' locations to achieve the integral length ratio criterion, and this may prompt us to perform a local smoothing process, a regular hexahedral mesh was generated using the Ansys meshing software, detailed Explanation of Figure 6 and Simulation Setup.

Figure 6 illustrates the mesh used in modeling the domain surrounding the studied body (cylinder), with a clear focus on refining the mesh cells in the critical regions where vortices form upstream, downstream, above, and below the body, it is observed that the cells are very close to the cylinder's surface, achieving a level of refinement that ensures a $y^+ \leq 1$, which confirms the mesh's ability to capture the fine details of the boundary layer, including its separation moments and vortex formation, the y^+ value is an indicator of the proximity of the mesh cells to the surface; values less than 1 mean that the cells penetrate the viscous sublayer, allowing for accurate simulation of phenomena such as surface shear stress and pressure fluctuations associated with vortices.

The process of cell refinement extends to the regions surrounding the entire cylinder, not just in the traditional areas behind the body (like the wake region), to ensure a comprehensive representation of the flow interaction with the surface in all directions, this detail is necessary for simulating the phenomenon of "vortex-induced vibrations" (VIV), where the vortices formed on different sides of the body affect it asymmetrically, generating time-varying lift and drag forces that cause vibrations.

Regarding the flow conditions, an air stream with a velocity of 5 {m/s} and a temperature of 22° {C} is applied, placing the Mach number below 0.3, and thus the fluid (air) is considered incompressible, this assumption is used to simplify the governing equations (such as the Navier-Stokes equations) without neglecting the fundamental hydrodynamic effects, the physical properties of air (such as viscosity and density) are derived from the software's default settings, which are usually based on standard air values at the mentioned atmospheric conditions.

The mentioned mesh accuracy is directly related to the accuracy of the boundary conditions (illustrated in Figure 7), such as defining the inlet velocity, outlet pressure, and the "no-slip" condition on the cylinder's surface, these settings allow for a realistic simulation of the energy transfer from the air stream to the vibrating body, which is crucial in evaluating the performance of resonant wind generators, such the ability to capture the precise moment of vortex

separation from the surface contributes to understanding how the kinetic energy of the wind is transferred to mechanical energy in the column, and then to electrical energy through the conversion systems.
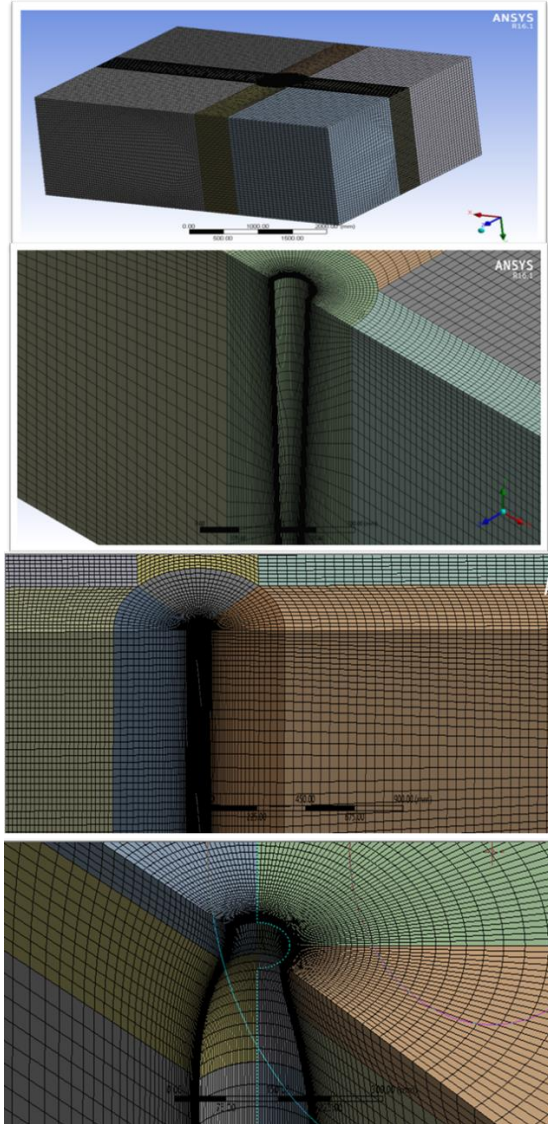

Fig. 6. Mesh the domain of the studied models

Finally, this setup highlights the importance of the integration between mesh accuracy and fluid properties in modeling the two-way fluid-structure interaction (FSI), where errors in representing the boundary layer or neglecting vortex formation regions contribute to inaccurate results for estimating the generated energy.

5. SOLUTION STRATEGY AND MODEL VALIDATION

It is not possible to reach a correct and stable solution using the turbulence model LES directly, but there are steps that should be followed to reach this solution without problems related to the stability and convergence of the solution, these steps are summarized by solving the RANS equations (the
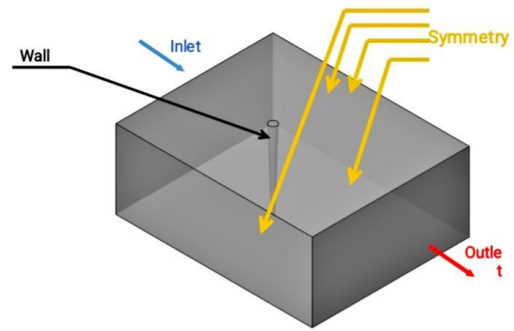

Fig. 7. Boundary conditions

equations for the conservation of mass and momentum and one of the turbulence models) by using a coarse mesh in the steady state. Using the pseudo transient, then the SIMPLE algorithm, followed by moving to the transient state and taking the resulting solution as initial values for the subsequent solution, the RANS equations are solved using a smooth mesh in the transient state, where the previous solution should be taken as initial solution conditions, and during the solution the program should be stopped in order to monitor the values of each courant number $C_o \leq 1$, the integral length ratio $R_l = 5 - 10$, and $y^+ \leq 1$ as previously mentioned, the performing of the smoothing mesh based on adaption within the Fluent software, adjusting the time step until reaching the limits of those values. When the previous values are reached, the LES turbulence model will be started, second-order spatial and temporal interpolations were adopted for the basic equations, and the convergence of the solution at values of the residuals less than 10^{-4} for all equations were taken, in order to verify the validity of the solution, the numerical results obtained from reference [18] were compared, in this study, flow around a cylinder was modelled at Reynolds number $Re = 10000$ and the numerical results were compared with the experimental results, and agreement was reached between the experimental results and the numerical result, t shows a comparison between the values of the lift and drag coefficients and the Stroll number in the current study and Reference No. [18], and the relative error value between the two studies.

Table 1. Comparison of data with the study in reference 14 in order to validate the solution

	Cl(RMS	Cd	St
Nguyen LTT and Temarel P (3D-LES)	0.793	1.63	0.27
Current study	0.77302	1.61	0.254
relative error	%2.51	1.22%	7.2%

The change in the value of the lift coefficient to validate the FE models shows the fast Fourier

transformer of this signal, the frequency value, and the value of the Stroll number.

6. RESULTS AND DISCUSSION

6.1. Flow field of the studied models

As a result of changing the nature of the flow field and the accompanying moving vortices within this field, the diagrams of flow variables such as pressure, velocity, etc. will not reflect the large difference between these models, the cases studied have a great precision due to the presence of uncertainty at the time when the modelling stopped and the time when the solution began to stabilize; however, the models have no useful in showing the nature of the flow, the mechanism of forming vortices, and its relevance to the components of speed and pressure. What is important later is the statistic and average analyses of the components of the forces acting on the surface of the cylinders, coefficients of lift and drag, and the frequency of the lift force in particular, because it is an oscillating force with a specific frequency, which results in the vibrating movement of the cylinder, all values of flow field variables (velocity and pressure) were shown for the studied models in two perpendicular sections in the middle of the field at the y=1 plane and Z=0 plane, *f* and Fig. 9 showing the values of the velocity diagrams, a successive Carmen street of sequential vortices that form and move behind the body, away from it, until it disintegrates and disappears in the end.
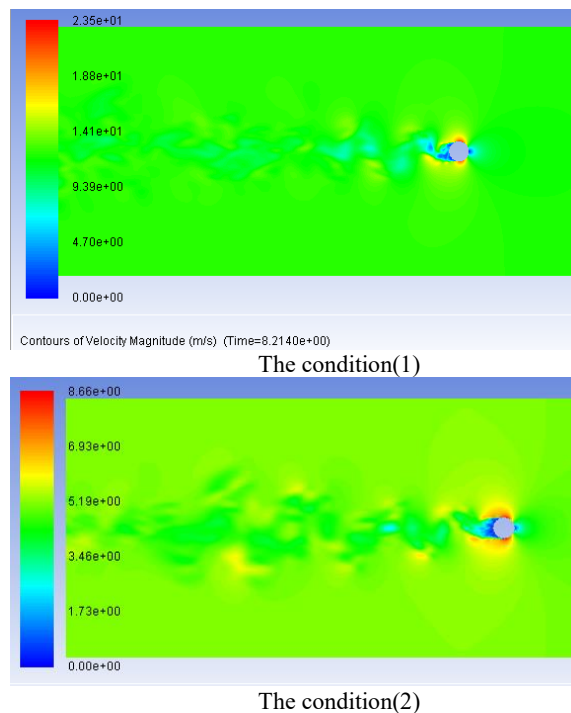

The condition(1)

The condition(2)
Fig. 8. Velocity contours at y=0

The condition(1)
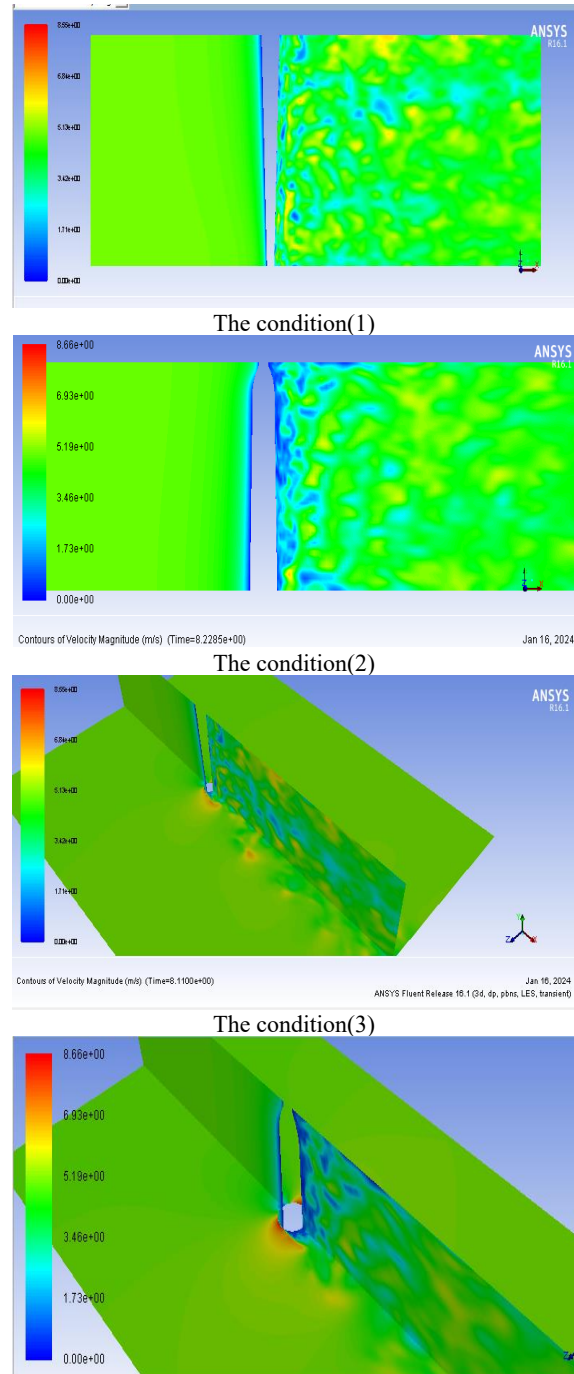

The condition(2)

The condition(3)

The condition(4)
Fig. 9. Velocity contours at z=0

It has been noticed that for each cycle (the movement of the body up and down), two single vortices are formed, rotating in opposite directions and soon separating from the body, the previous figures showed that there are regions of high velocity surrounding the low velocity region, correspond to places where the flow slows down in a vortex manner, there is no significant change in the velocity field values between the models (case A and B), as can be seen in Figure 10, it has been noticed that there is a larger area behind the surface of the body in the second model with more low speed values, and this constitutes a large imbalance in the pressure behind the surface of the body in the second model, this

increases the nature of the turbulence in the flow, and in turn increases the possibility of delaying the separation of the boundary layer, thus, the drag resistance decreases and the values of the lift force increase, this can be confirmed from the pressure diagrams of the two models shown in Figure 10, it also showed red areas of high pressure at the front of the body, which corresponds to an area where the flow stops (stagnation point), and the flow begins to accelerate after that, it has been noticed that the vacuum pressure values behind the body are larger in the second model compared to the first.

Fig. 10 shows that, during the shedding of the vortex, areas with a low value of alternating pressure are formed on both sides of the cylinder. Every time the vortex separates from the wake as a result of the instability of the flow, it leaves its place in the area with a high pressure gradient, which is the driving force in the flow, and the pressure value is low.

By showing the velocity vector diagrams Fig. *11* it is possible to observe the location and the beginning of separation of the boundary layer due to the positive pressure gradient, it is also possible to observe the formation of two upper and lower vortices moving in opposite directions, it should be noted that these two vortices do not form together, when one of them grows (forming a vortex); the second becomes smaller (vortex shedding) and when they reach a specific value they peel off from the surface of the cylinder and move with a specific time interval equal to the period of vibration resulting from this phenomenon, F also shows this phenomenon for the second model (Case B) the image corresponds to a time when the two vortices were equal, after that, one of them became smaller and the other became larger.

Figure 12 displays the results of the Fast Fourier Transform (FFT) analysis of the vortex shedding phenomenon in the second model (Case B), highlighting the presence of a single dominant frequency that governs the motion of the vortices and the timing of their separation from the horizontal surface of the body, this frequency is closely linked to the interaction between the structural characteristics of the body (such as its natural frequency) and the flow characteristics (such as wind speed and the Strouhal number (St)).

By comparing these results with Figure 11, which documents the evolution of the size of the two vortices over time, we observe that the dominant frequency in Figure 12 explains the transition from a phase of symmetry between the vortices (where they are equal in size) to a phase of asymmetry (where one becomes larger than the other), this indicates that the dominant frequency is not merely a random outcome, but rather a product of a lock-in mechanism between the vortex shedding frequency and the body's natural vibration frequency. When one of the vortices begins to inflate at the expense of the other (as in Figure 11), the dominant frequency emerges as a clear signal in the FFT spectrum (Figure 12), confirming the control

of this frequency over the dynamics of the entire system.

The relationship between the dominant frequency and energy generation efficiency is crucial here: in resonant wind generators, the goal is to achieve resonance between the vortex shedding frequency and the natural frequency of the column. Figure 12
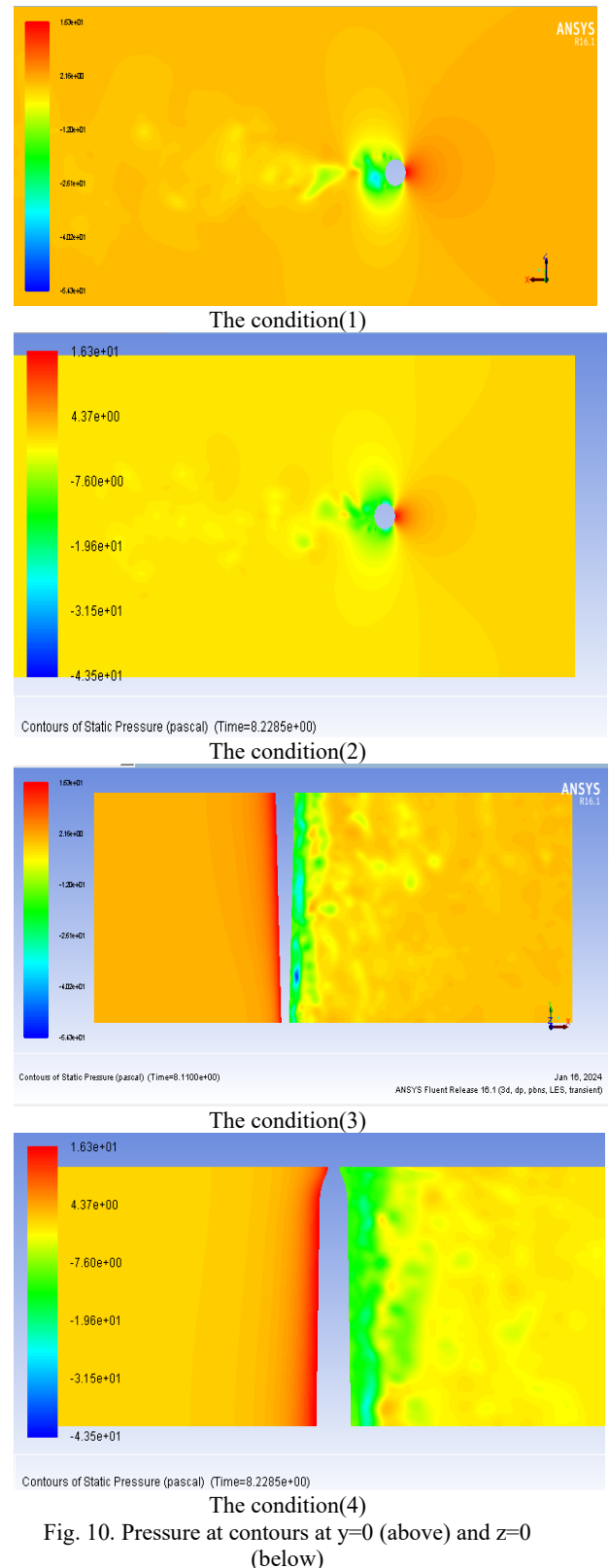

The condition(1)

The condition(2)

The condition(3)

The condition(4)

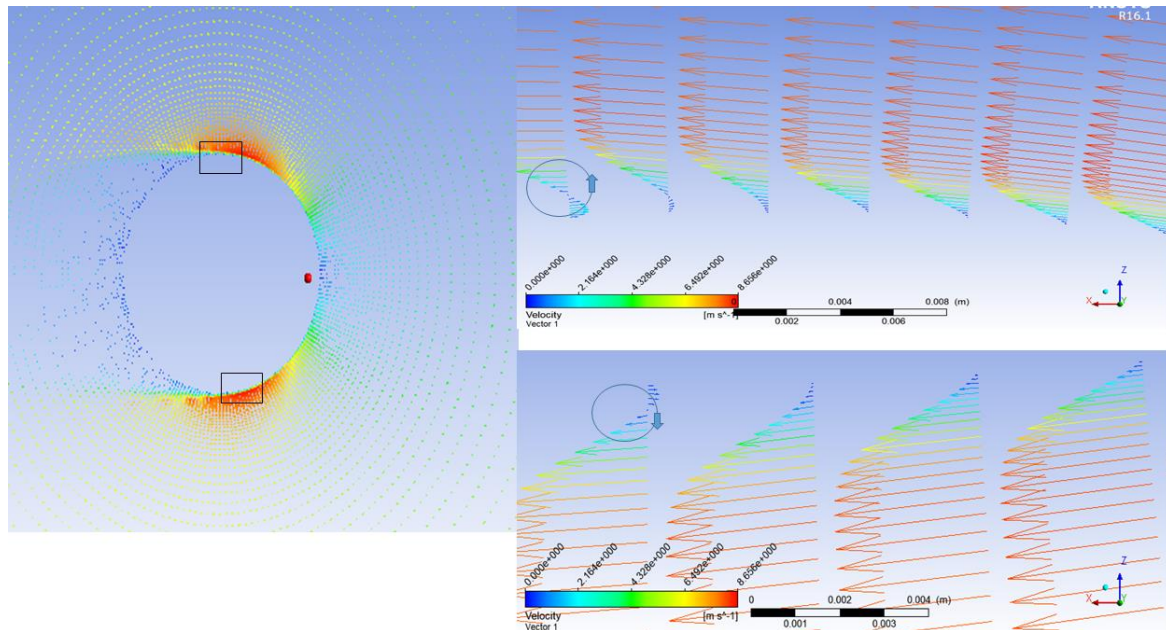Fig. 10. Pressure at contours at y=0 (above) and z=0 (below)

Fig. 11. Velocity vectors.

shows that the dominant frequency falls within the range that achieves this resonance, even with variations in the size of the vortices, this explains why energy generation continues with relative efficiency despite the fluctuations in vortex formation, as the dominant frequency acts as an "attractor" that reorganizes the apparent chaos in Figure 11 into a regular pattern exploitable for energy.

Finally, the absence of strong side frequencies in Figure 12 indicates that the design of the second model (Case B) successfully reduced unwanted frequency interferences, which could weaken energy transfer, this result confirms the effectiveness of the design modifications (such as changing the column's cross-section) in improving the stability of the vortex-induced vibrations, which is crucial for the application of this technology in varying climatic conditions.

6.2 Dynamic response study

After obtaining the results of the numerical modelling of the flow field around the two models; a one-way fluid–structure interaction coupling between the flow field and the solid body will be conduct, in this case, we take into account the effect of the flow field on the body immersed in the fluid without the effect of the movement of the solid body immersed in a fluid on the flow field i.e., tow-way FSI because the other cases are very computationally expensive and is not important when the shape of the body is rotationally symmetric, the amplitude of the vibration is not affected by the angle of attack, as in the case of self-stimulation phenomenon of vibration i.e., Galloping.

The values of the basic mechanical properties of the material from which the body of the two models

were made have been entered at first, by following the same procedure in a number of previous researches [10], and defined within the materials library of the Ansys Workbench software, where materials made of Glass Fiber were used, t shows the most important of these properties:

Table 2. Glass fiber properties

2440	Kg/m^3 density
68.9	GPa Young's Modules
0.183	Poisson's ratio

Secondly, the values of the natural frequencies of the two studied models were calculated based on the finite element method (FEM) by solving the general equation of motion without the presence of any external forces using the Ansys Modal Shape software, and the simulation results are presented in Figure 13.

The value of the natural frequency of the first model is slightly greater than the frequency of the second model, with a maximum displacement of the first model that is greater compared with the second one, it is important not to confuse this displacement with the displacement resulting from the flow field, as this is a random displacement to calculate the natural frequency, the value of the natural frequency may have a slightly change when the body is under the influence of lateral compressive or tensile loads, as the value of the body's natural frequency decreases by 5% when it is under compressive load, while it increases by 5% when it is under tensile load, in this study this small change in the natural frequencies of the models have been neglected.
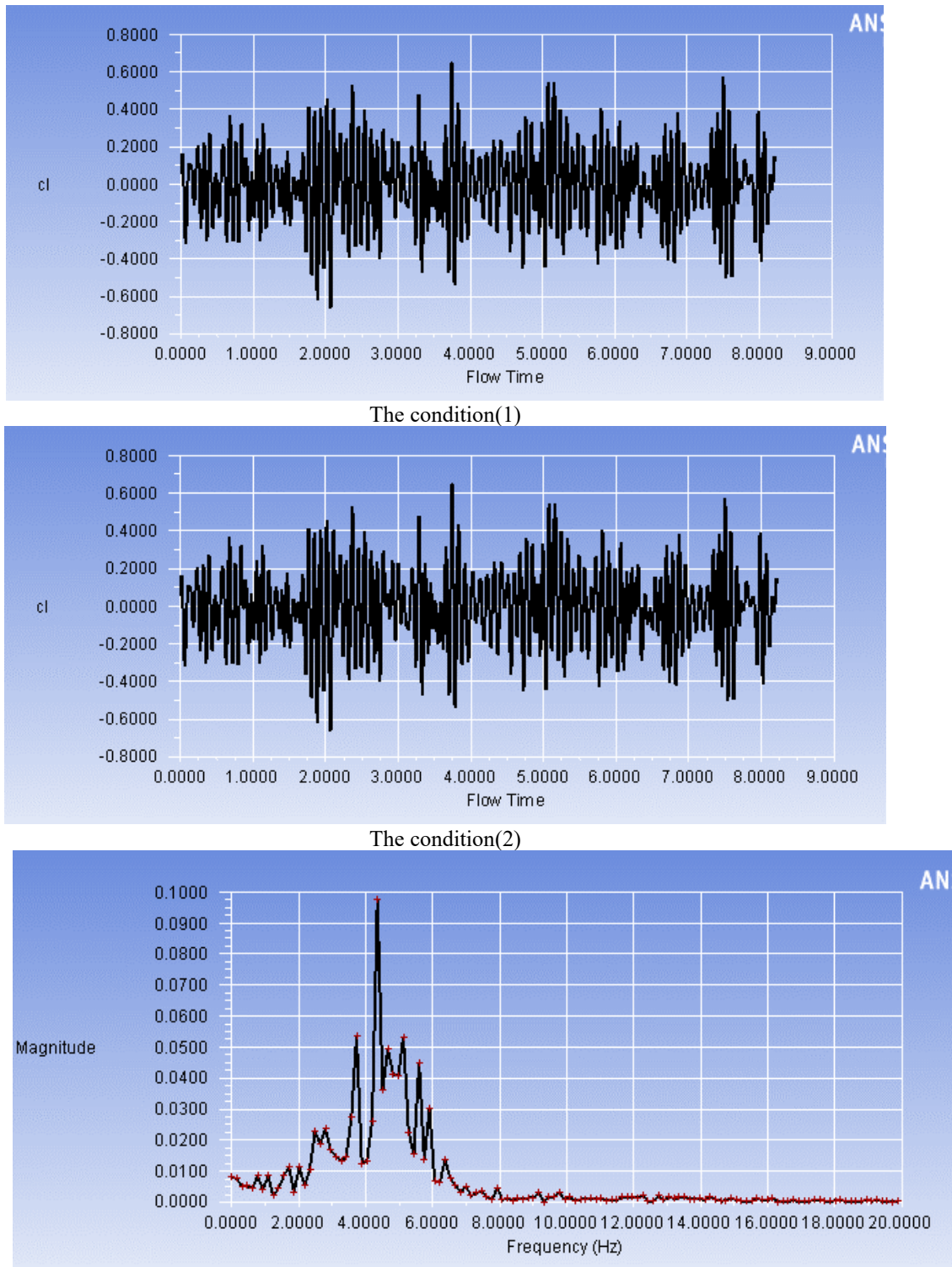
The condition(1)

The condition(2)

Fig. 12. The value of the lift and frequency coefficient for the studied models

Whereas Cl_o is the average amplitude of the lift coefficient, and RMS the root mean square of the values, f_s vibration frequency resulting from the flow, and f_n represents the natural frequency of the body, while FR is the ratio of the vibration frequency to the natural frequency, the closer to the resonant frequency and then gives better response, Fig. 14 Case B has the lower frequency by 2.3% compared with the model A; Therefore, it is the best.

The results of numerical modelling of the flow field with the value of natural frequencies for the two studied models can be summarized in fig. 13.

By comparing the values of the aerodynamic characteristics in table 3, there is a decrease in the value of the average drag coefficient in the second model compared to the first at the same air speed of 5 m/sec by around 34%, and an increase in the lift coefficient Cl (RMS) by 49.3%, there is a noticeable
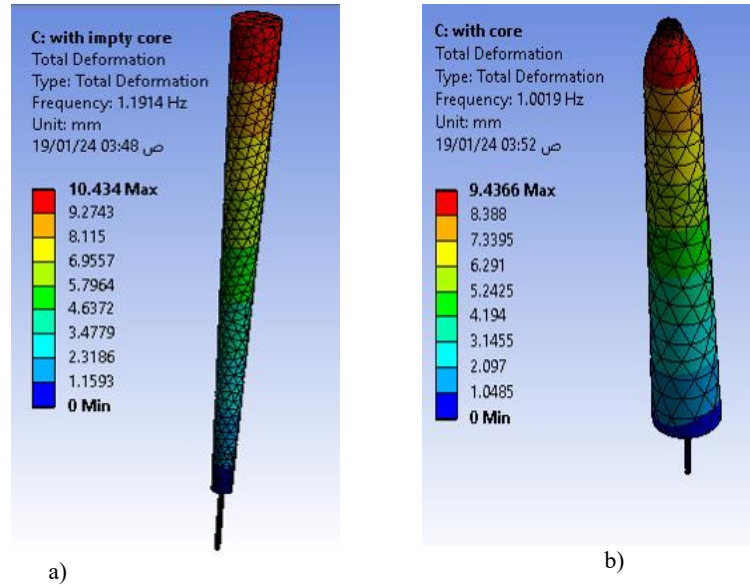
Figure 13. Natural frequencies for studied models: a) the condition (1), b) the condition (2)

Table 3. Numerical simulation results

$FR = f_s/f_n$	f_n (Hz)	f_s (Hz)	Cd (Ave)	Cl_o	Cl(RMS)	model
4.448	1.1914	5.3	1.164	0.452	0.32	A
4.342	1.0019	4.35	0.769	0.675	0.478	B

improvement in aerodynamic performance compared between the two models, and this result can be understanding by recognizing the fact that the new geometric shape is characterized by a larger flow area and form more turbulence intensity, this in turn reducing the drag forces and delays the separation of the boundary layer, and raising the values of the lift coefficient.
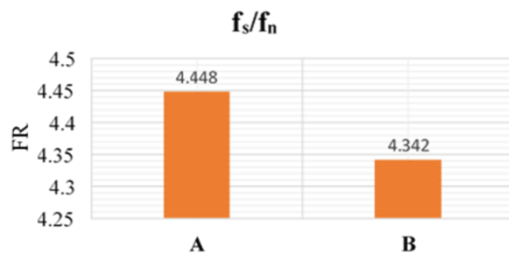

Fig. 14. Comparison of the frequency ratio of the studied models.

The RMS and amplitude values of the lifting force and the average drag value were calculated from the values obtained from the modelling, at this stage, the frequency response of these models will be studied in the cases mentioned.

Where a force applied in one direction due to the symmetrical shape of the studied models; the amplitude of this force is calculated based on the average amplitude of the lifting forces and the average value of the drag force according to the relationship $F_L = F_{l(Amplitude)} sin(\omega t)$, and the frequency response values are calculated using Ansys dynamic response software.

Fig. 15 showing the calculated frequency response diagrams according to the time-based average method for the damping ratios and plotted on the logarithmic y-axis and the linear x- axis, all the previous damping ratios have no much differences, however, the response varies when the period of vibration matches the natural vibration frequency of the analyzed body, it is also possible from these diagrams to deduce the amplitude of the vibration in the studied cases.

7. POWER CALCULATIONS

In order to evaluate the best performance among the two studied models; the mechanical power resulting from each of the models should be calculated based on the RMS values, the power values resulting from vibration are shown in Table 4.

The previous table showed the values of the resulting power, and the power value at the studied air speeds is a very small, and its values are approximately not affected by the presence of damping, the power value is infinite at resonance with the absence of any damping, and it is the ideal state that cannot be achieved in practice. However, when taking the real state at resonance, taking damping into account, the term $\left(1 - \left(\frac{f_s}{f_n}\right)^2\right)^2$ becomes not existent in the power equation, and the power becomes proportional to the term $\frac{1}{\xi}$, that is the changes become a part of an hyperbola that have asymptote $\xi = 0$. By comparing
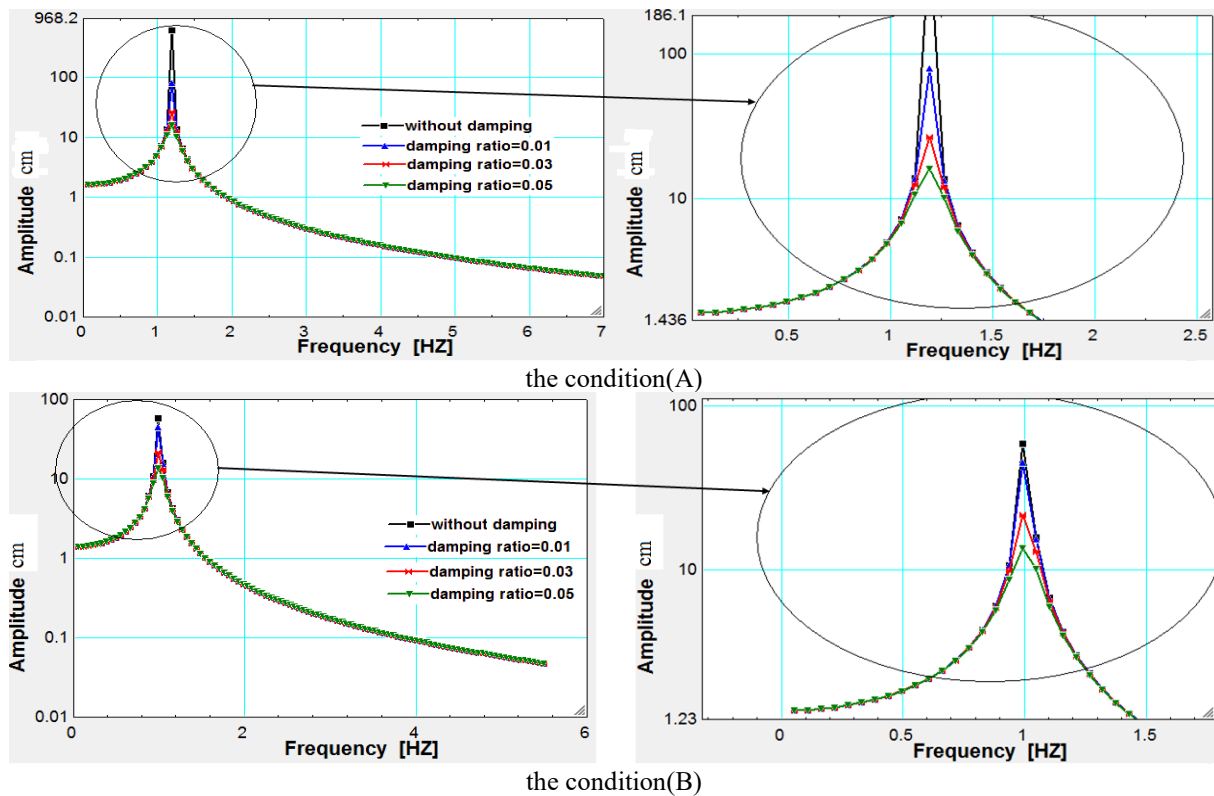
the condition(A)

the condition(B)

Fig. 15. Frequency response of model A and B

Table 4. power calculation results

Case A			Case B		
P[W]			P[W]		
Damping ratio	Actual value Hz	Value at resonant Hz	Damping ratio	Actual value Hz	Value at resonant Hz
0	3.658	inf	0	16.858	inf
0.01	3.652	77	0.01	16.853	552
0.0 3	3.649	25	0.03	16.845	184
0.05	3.645	15	0.05	16.839	110

the power values between the two studied models, there is an improvement in the power value in the second studied model compared to the first, since the power increased in the second model at the studied air speed, the frequency of the second model does not match the resonance by 361%, that is approximately three and a half times the resonance with a damping ratio of 0.05, the power increased by 633%, or almost 6 times, and this increase isa result of two factors: The first is an improvement in the aerodynamic performance of the second model compared to the first one, as previously discussed, the improvement of the lift coefficient by 50% and the decrease in the drag coefficient by 34%, the second model has a decrease in frequency compared to the first model by 2.3%.

This suggests that the design modifications implemented in the second model (Case B) not only improved the aerodynamic coefficients (as discussed previously) but also resulted in a more efficient energy extraction mechanism even when the vortex shedding frequency (f_s) is not perfectly aligned with the natural frequency (f_n), the table highlights a crucial aspect of resonant systems: the dramatic increase in power output near resonance, especially with minimal damping.

While an infinite power output at perfect resonance with zero damping is theoretically ideal but practically unattainable, the trend clearly indicates the sensitivity of power generation to the proximity of f_s to f_n and the level of damping xi .
The fact that Model B exhibits a substantial power increase (633%) despite its operating frequency being significantly off-resonance (by 361%) with a damping ratio of 0.05 underscores the effectiveness of its design in capturing and converting wind energy into mechanical vibrations, this improvement likely stems from a combination of factors, including the optimized aerodynamic profile leading to stronger and more consistent vortex shedding, and

potentially a more efficient structural response that translates these vibrations into usable power, this observation suggests that while achieving perfect resonance is desirable, a well-designed resonant wind generator can still offer significant performance advantages even when operating slightly away from its ideal resonant frequency, provided that the aerodynamic forces are sufficiently enhanced and the structural damping is controlled, the substantial power increase in Model (B), despite the frequency mismatch, indicates a more robust and efficient energy harvesting capability compared to Model (A) under the same operating conditions, this finding further supports the benefits of the design modifications incorporated in the second model.

8. DISCUSSION

The results of this study demonstrated a notable improvement in the performance of the second model (Case B) compared to the traditional model (Case A), with a 34% reduction in the drag coefficient (C_d) and a 49.3% increase in the root mean square of the lift coefficient ($C_{l_{RMS}}$), which aligns with similar improvements in previous studies on resonant wind generator designs, for instance, study [2] indicated that the use of composite materials and the modification of the geometric shape of columns reduce drag resistance and enhance vortex-induced vibrations, which explains the decrease in C_d in Model B, study [6] also confirmed that the increase in the lift coefficient is associated with achieving frequency synchronization (Lock-In) between the vortex shedding frequency and the natural frequency of the body, which is evident in the significant increase in $C_{l_{RMS}}$ when the frequencies match in Figure 12.

On the other hand, the current study showed that the tapered column design in Model B led to a delay in boundary layer separation, which increased the stability of the vibrations, this finding is consistent with the results of study [3], where changing the cross-section of the column improved pressure distribution and reduced energy loss, study [12] also showed that conical columns improve the synchronization of vortices with the natural frequency, which supports the decrease in the frequency ratio ($FR = \frac{\{f_s\}}{\{f_n\}}$) in Model B (Table 3). Regarding the dynamic response, Model B exhibited a 2.3% lower natural frequency compared to Model A (Figure 14), which is attributed to its larger mass and improved material distribution, this observation is consistent with the findings of study [10], which showed that the natural frequency is significantly affected by mass distribution and material stiffness, the significant increase in generated power (633% in Model B) is also similar to what was mentioned in study [11], where structural modifications led to the amplification of the vibration amplitude and enhanced energy transfer.

It is worth noting that the decrease in back pressure (vacuum) values in Model B (Fig. 10) reduces drag resistance, which is consistent with the analyses of study [17] on the effect of back pressure on C_d. Likewise, the absence of strong side frequencies in the FFT spectrum (Figure 12) indicates the efficiency of Model B's design in avoiding frequency interferences, which was supported by study [8] in the context of improving vibration stability, finally, the use of one-way FSI modeling in this study is considered a limitation compared to studies such as [18] and [19], which used two-way interactions.

However, the results are still comparable to the work of [20], which confirmed that simplifications in modeling do not weaken accuracy when studying rotationally symmetrical bodies.

9. CONCLUSION

In this study, the effect of modifying the profile design of two models on aerodynamic performance and the frequency response was analyzed, the was analyses have been carried out by modelling the unilateral fluid –structure interaction between the fluid and the solid body using Ansys 16.1, the study led to the following conclusions:

- A faster rate of span and expansion of the generated vortices in the second model compared to the first model, this explains the improvement of the aerodynamic properties of the second model since the intensity of the turbulence of the flow increases in the second model, this delays the separation of the boundary layer and thus improves the lift coefficient and reduces the drag force (friction).
- The frequency ratio for the second model decreased compared to the first model by 2.3%, and therefore it is the best.
- There is a decrease in the value of the average drag coefficient in the second model compared to the first model at the same speed of 5 m/sec by 34%, and an increase in the lift coefficient Cl (RMS) by 49.3%, this means a noticeable improvement in aerodynamic performance of the second model compared to the first one.
- By comparing the power values between the two studied models, there is an improvement in the power value in the second model compared to the first, at the same air speed and the frequency does not match the resonance by 361%, that is, approximately three and a half times, as for resonance with a damping ratio of 0.05; the power increased by 633%, almost 6 times.

Author contributions: *research concept and design, H.F.L., Collection and/or assembly of data, H.F.L.; Data analysis and interpretation, H.F.L., A-B.J.H.; Writing the article, A-B.J.H.; Critical revision of the article, H.F.L., S.M.M.; Final approval of the article, A-B.J.H., S.M.M.*

Declaration of competing interest: *The authors declare that they have no known competing financial interests or personal relationships that could have appeared to influence the work reported in this paper.*

REFERENCES

1. Al-Bedhany Jasim H, Tahseen Ali Mankhi, Legutko S. A surface study of failed planetary wind turbine gearbox Bearings to investigate the causes of the Bearing premature failure issue. Heliyon. 2024. https://doi.org/10.1016/j.heliyon.2024.e25860.
2. Onkar D Kshirsagar, Gaikwad AB. Design and analysis of vortex bladeless windmill for composite material. Journal of Industrial Mechanics. 2019;4(2). http://doi.org/10.5281/zenodo.3355094.
3. Thorpe T. A brief review of wave energy. Technical reportno. R120. Energy technology support unit (ETSU) a report. 1999:1-27.
4. Duckers L. Wave energy. In Renewable Energy (Ed. G.Boyle), 2nd edition, (Oxford University Press, Oxford, UK). 2004, Ch. 8.
5. Benjamin D, Plummer AR, Sahinkaya MN. A review of wave energy converter technology. 2009:887-902. https://doi.org/10.1243/09576509JPE782.
6. Villarreal DJY. VIV resonant wind generators. Vortex Bladeless S.L. 2018.
7. Raut P, Sawant T, Raul M, Shingade M. Design & CFD analysis of bladeless wind turbine. Journal of Applied Science and Computations. 2019;VI(III).
8. Sabab MW, Mohd S. Aerodynamic characteristic of vortex bladeless wind turbine. Universiti Tun Hussein Onn Malaysia, Johor, Malaysia. 2021. https://doi.org/10.30880/rpmme.2021.02.01.021.
9. Gaurao G, et al."Study of vortex induced vibrations for harvesting energy. International Journal for Innovative Research in Science & Technology. 2016: 374-378.
10. Harshith K, Santosh B. Bladeless wind power generation. International Journal of Scientific Research and Development. 2016:66-73.
11. Elsayed AM, Farghaly MB. Theoretical and numerical analysis of vortex bladeless wind turbines. Wind Engineering. 2022;46(5):1408-1426. https://doi.org/10.1177/0309524X221080468.
12. Barrero-Gil A, Santiago P, Sergio A. Extracting energy from vortex-induced vibrations: a parametric study. Applied mathematical modelling. 2012;36(7): 3153-3160. https://doi.org/10.1016/j.apm.2011.09.085.
13. Fluent ANSYS. Ansys fluent theory guide. Ansys Inc., USA 15317. 2011:724-746.
14. Wang C, et al. CFD simulation of vortex induced vibration for FRP composite riser with different modeling methods. Applied Sciences. 2018;8(5):684. https://doi.org/10.3390/app8050684.
15. Raut HS, Harish ND. Vortex shedding patterns in flow past a streamwise oscillating square cylinder at low Reynolds number using dynamic meshing. Physics of Fluids. 2019;31(11). https://doi.org/10.1063/1.5123347.
16. Khosrow B, Tamimi V, Zeinoddini M. VIV of tapered cylinders: 3D LES numerical simulation. International Journal of Maritime Technology. 2015;3:17-31. https://dor.isc.ac/dor/20.1001.1.23456000.2015.3.0.2.4.
17. Achenbach E, Heinecke E. On vortex shedding from smooth and rough cylinders in the range of Reynolds numbers 6×10^3 to 5×10^6. Journal of fluid mechanics. 1981;109:239-251. https://doi.org/10.1017/S002211208100102X.
18. Pandeli P. Numerical simulation of an oscillating cylinder in cross-flow at a reynolds number of 10,000: Forced and free oscillations. ASME 2014 33rd International Conference on Ocean, Offshore and Arctic Engineering. American Society of Mechanical Engineers Digital Collection, 2014. https://doi.org/10.1115/OMAE2014-23394.
19. Dogus AH, Elvin N, Andreopoulos Y. The performance of a self-excited fluidic energy harvester. Smart materials and Structures 2012;21(2):025007. https://doi.org/10.1088/0964-1726/21/2/025007.
20. Turgut S. Vortex-induced oscillations: a selective review. 1979:241-258. https://doi.org/10.1115/1.3424537.

Lecturer **Firas Lattef Hussany,** M.Sc. in Mechanical Engineering from Firdowsi of Mashhad,; 2018; Researcher in Mech. Eng. Department, The University of Misan; Iraq
e-mail: firaslattef@uomisan.edu.iq

Assistant Professor *Jasim Hasan Ilik AL-Bedhany.* M.Sc. Mechanical Engineering, University of Baghdad, 2009, Baghdad, Iraq and Ph.D from the University of Sheffield UK,; 2020; Researcher and Lecturer in Mech. Eng. Department, The University of Misan; Iraq.
e-mail: j.h.al-bedhany@uomisan.edu.iq

Dr. **Mahmood Shakir Mahmood**, Head of Mechanical Engineering Dept. M. Sc. from the University of Basrah; Iraq and Ph.D. from the University of Basrah, Iraq; 2023; Researcher in Mech. Eng. Department, The University of Misan; Iraq.
e-mail: mahmood-shacker@uomisan.edu.iq